POLITECNICO DI TORINO
Repository ISTITUZIONALE

Hardware-in-the-Loop Assessment of a Data-Driven State of Charge Estimation Method for Lithium-Ion Batteries in Hybrid Vehicles

(Article begins on next page)

18 October 2022

Article

Hardware-in-the-Loop Assessment of a Data-Driven State of Charge Estimation Method for Lithium-Ion Batteries in Hybrid Vehicles

Sara Luciani [ID], Stefano Feraco *[ID], Angelo Bonfitto [ID] and Andrea Tonoli [ID]

Department of Mechanical and Aerospace Engineering, Politecnico di Torino, 10129 Torino, Italy; sara.luciani@polito.it (S.L.); angelo.bonfitto@polito.it (A.B.); andrea.tonoli@polito.it (A.T.)
* Correspondence: stefano.feraco@polito.it; Tel.: +39-011-0906239

Abstract: This paper presents the design and hardware-in-the-loop (HIL) experimental validation of a data-driven estimation method for the state of charge (SOC) in the lithium-ion batteries used in hybrid electric vehicles (HEVs). The considered system features a 1.25 kWh 48 V lithium-ion battery that is numerically modeled via an RC equivalent circuit model that can also consider the environmental temperature influence. The proposed estimation technique relies on nonlinear autoregressive with exogenous input (NARX) artificial neural networks (ANNs) that are properly trained with multiple datasets. Those datasets include modeled current and voltage data, both for charge-sustaining and charge-depleting working conditions. The investigated method is then experimentally validated using a Raspberry Pi 4B card-sized board, on which the estimation algorithm is actually deployed, and real-time hardware, on which the battery model is developed, namely a Speedgoat baseline platform. These hardware platforms are used in a hardware-in-the-loop architecture via the UPD communication protocol, allowing the system to be validated in a proper testing environment. The resulting estimation algorithm can estimate the battery SOC in real-time, with 2% accuracy during real-time hardware testing.

Keywords: battery monitoring system; state of charge; artificial neural networks; hardware-in-the-loop; real-time hardware; modeling

1. Introduction

In response to current growing worries about global warming and the increasing scarcity of natural resources, the need for more efficient cars is, thus, strictly linked to even more stringent regulations about fuel economy, emissions, and energy consumption [1]. In the automotive sector, this process has resulted in the creation of incentives to concentrate on novel alternative powertrain technologies [2]. In this framework, batteries have gained wide interest for being crucial to fully electric, hybrid, and plug-in hybrid cars (BEVs, HEVs, PHEVs). Specifically, lithium-ion batteries are mostly used in automotive applications, due to their impressive characteristics, such as high-energy density, low self-discharge rate, rapid charging time, and efficient power output [3–5]. Nevertheless, battery performance and health are influenced by charging/discharging cycles and environmental variables, which can all affect the battery dynamics [6].

Since EVs are not ready to be sold on a large scale in the next few years, according to [7], new solutions need to be developed to meet the targets that have been established for emission reduction. Therefore, HEVs are gaining important interest worldwide because they combine an electric energy storage unit, i.e., the battery, with an electric motor and a device that couples the electric and thermal drivelines. As described in [8,9], the combination of the two propulsion systems allows the vehicles to achieve better performance, in terms of both engine usage and fulfillment of the power request. According to the mechanical architecture, most HEVs can be roughly divided into six categories: micro/mild parallel,

full parallel, series, combined, power split, and through-the-road (TTR) hybrids [10]. Specifically, in a series HEV, the power sources supply electrical energy to a DC bus. Parallel HEVs can use the internal combustion engine (ICE) or electric machine (EM) alone or together. Regenerative braking uses the EM to charge the battery. Parallel mild HEVs are suitable because they provide a good balance between cost and performance. Complex HEVs combine parallel and series architecture. Except for the motor's power flow, which is bidirectional in complex hybrids and unidirectional in series–parallel HEVs, they are essentially identical to series-parallel HEVs. Among all these architectures and designs of hybrid powertrains, which are currently under development, a lot of research has been devoted to 48 V batteries, as it can make the electric driveline capable of recovering more energy in short periods of time from braking action, with respect to 12 V layouts, while being easily integrated in the electrical systems of the vehicle, as stated in [7,11].

Despite the advantages of 48 V hybrid architecture, the battery *SOC* remains a crucial quantity, which can be estimated via the measurement of other battery parameters, such as voltage, current, and temperature. In detail, *SOC* estimation often relies on the direct measurement of open circuit voltage, internal impedance, or integration of the current over time [12,13]. Under controlled laboratory conditions, these techniques are accurate, although they can be energy consuming and not applicable during the vehicle motion in real-time applications, as stated in [14]. Many approaches have been investigated in the recent literature to overcome those issues, such as model-based, rule-based, and artificial intelligence (AI) methods. The Kalman filter (KF) [15], extended Kalman filter (EKF) [16–19], unscented Kalman filter (UKF) [20,21], adaptive particle filter (APF) [22], and smooth variable structure filter (SVSF) [23,24] are included in the first category. On the contrary, rule-based algorithms, such as fuzzy logic (FL) [25–27], are model-less techniques that are mostly reliant on the expertise of the designer.

In recent research studies, AI-based techniques and, more specifically, the application of ANNs, have gained a great momentum in representing nonlinear dynamics in real-time applications, such as the *SOC* estimation, as discussed in [28,29]. The ANNs can guarantee online estimation and estimate the *SOC* using discrete life span of the battery, instead of the whole life span. The impact of the battery temperature effects can also be considered. Nevertheless, the accuracy of an ANN is heavily influenced by the selection of a proper input/output layout and an adequate training dataset. A large amount of data is needed to train the algorithm, and the precision depends on the accuracy of the model applied to experimental datasets. Among all the ANN architectures that are used in the literature for battery *SOC* estimation [30,31], the NARX model is used in this work, since it has been proven to be accurate and robust in a prior work by the authors [28]. Furthermore, considering a battery working condition at a quasi-constant temperature, the present work investigates two different layouts for the retained NARX ANN: the first one includes only two inputs, i.e., the instantaneous values of current and voltage, whilst the latter includes four inputs, including the averaged quantities of those values, as performed in [32] for a different ANN model.

Out of all the potential estimating methods, this methodology is the most effective at capturing the non-linear connection between various battery parameters, while minimizing the anxiety associated with uncertain EV operating conditions and the complicated electrochemical process of batteries [33,34]. Consequently, it does not require detailed physical knowledge of the battery, and the proposed layout ensures the deployment on a battery management system (BMS), due to the limited number of neurons and layers.

Both the proposed layouts are compared, in terms of estimation accuracy during different maneuvers performed on modeled driving cycles for a 48 V lithium-ion battery pack, namely during charge-sustaining and charge-depleting phases. In detail, the experimental validation is performed in a hardware-in-the-loop (HIL) configuration. To the best of the authors' knowledge, the real-time assessment of HIL implementation of *SOC* estimation ANN-based algorithms is limited to simple charge/discharge cycles that are not representative of real driving situations in HEVs [35]. Therefore, the proposed research work aims to

demonstrate that the proposed estimation algorithm can provide relevant results within the investigated experimental framework, ensuring that the proposed data-driven algorithm, based on NARX ANNs, can be rapidly deployed, tested, and validated on state-of-the-art hardware platforms.

In detail, the experimental validation process exploited a Raspberry Pi 4B card-sized board, in which the estimation algorithm is actually deployed, and real-time hardware, in which the battery model is developed, namely a Speedgoat baseline platform. These hardware platforms were used in the HIL architecture, via UPD communication protocol, allowing the system to be validated in a proper testing environment. Moreover, the considered battery system is a 1.25 kWh 48 V lithium-ion battery that is numerically modeled via an RC equivalent circuit model, which can also consider the environmental temperature influence.

In summary, the novel contribution of this work is the experimental validation of a data-driven *SOC* estimation method in a HIL configuration using the NARX ANN architecture. The investigated method is particularly addressed to the 48 V lithium-ion batteries used in actual HEVs. Moreover, the presented algorithm is validated during different real driving cycles and compares two estimation architectures that differ in the set of the retained inputs.

This paper is organized as follows. Section 2 illustrates the considered battery modeling approach, along with the hardware setup that is used for the HIL testing. This section also presents the ANN-based algorithm for *SOC* estimation in the two different layouts that are evaluated, in terms of accuracy. The used training dataset is finally illustrated. Section 3 presents and discusses the obtained results on the recorded datasets for the proposed HIL architecture. A performance analysis, in terms of estimation accuracy, is then presented. Finally, Section 4 concludes the paper.

2. Methodology

This section introduces the proposed battery modeling approach for the retained 48 V lithium-ion battery pack. Then, the designed experimental layout is presented, illustrating the HIL test architecture setup with both the considered hardware platforms, namely the Speedgoat baseline real-time target machine and a Raspberry Pi 4B card-sized board. The flowchart of the proposed approach is illustrated in Figure 1.
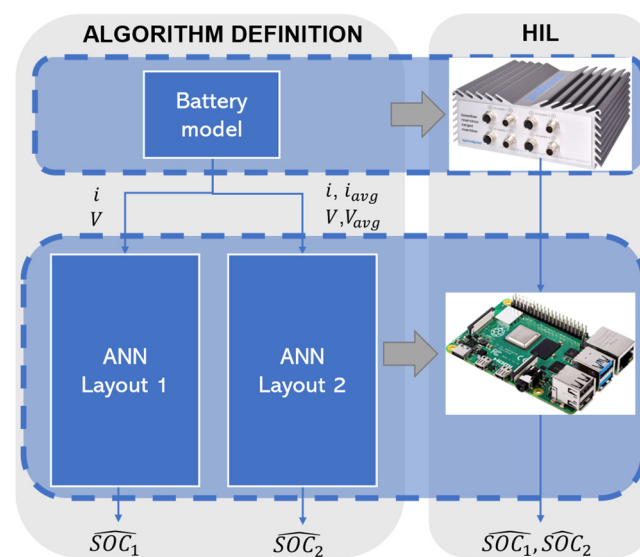

Figure 1. Flowchart of the proposed approach for the estimation of the *SOC*.

Eventually, the *SOC* estimation algorithm design and testing procedures are described in a dedicated subsection that illustrates the two considered ANN layouts. Moreover, the training algorithm and datasets are also discussed in this subsection.

2.1. Battery Modeling

This section aims to present the modeling of the battery pack in the Matlab/Simulink environment. The 48 V lithium-ion battery is modeled via an equivalent circuit model, considering some thermal effects. Many different battery models are investigated in the literature, and they could be distinguished in various categories, namely empirical, equivalent electrical circuit, and electrochemical models [36]. Empirical models provide a straightforward solution for quantitative comparisons of different operating situations, but their precision is low and cannot be utilized for exact performance evaluations. Conversely, mathematical models, based on the internal electrochemical reactions, are very accurate. Still, they require detailed knowledge of the battery chemical processes and can be difficult to deploy on embedded BMS. The usage of equivalent electrical circuit models is the most common technique exploited for simulating a battery's electrical performance [36,37].

This work considers a 14s11p configuration of cylindrical battery cells to model the entire battery pack. Each battery cell is made up of the series connection of an ideal voltage source, which represents the open-circuit voltage V_{oc} and is controlled by the *SOC* level, and a resistor R_0, which represents the internal resistance. The terminal voltage V_L could be expressed using Kirchhoff's voltage law, as follows:

$$V_L = V_{OC} - R_0 i_L \tag{1}$$

where V_{OC} and R_{OC} are obtained by interpolation:

$$V_{OC} = V_{OC}(SOC, T) \tag{2}$$

$$R_0 = R_0(SOC, T) \tag{3}$$

where T is the temperature vector $T = [-20, 0, 40]$ °C and *SOC* is an equally spaced vector between 0 and 1.

Moreover, the thermal behavior of the cell can be modeled by the following equation [32]:

$$mc_p \left(\frac{dT_{cell}(t)}{dt} \right) = hA(T_{amb} - T_{cell}(t)) + R_0 i_L(t) \tag{4}$$

where m is the mass of the battery cell [kg], c_p is the specific heat capacity [J/molK], h is the horizontal overall heat transfer coefficient [W/m²K], A is the surface area for heat exchange [m²], $T_{cell}(t)$ is the variable temperature of the battery cell [K], and T_{amb} is the ambient temperature [K].

In the Laplace domain, the battery cell temperature varies, according to:

$$T_{cell}(s) = \frac{R_{th}P_{loss} + T_{amb}}{\tau_{th}s + 1} \tag{5}$$

where R_{th} is the thermal resistance, cell to ambient [K/W], τ_{th} is the thermal time constant, cell to ambient [s], and $P_{loss} = R_0 i_L^2$ is the overall heat generated during the charge or discharge process [V]. Finally, the internal resistance (R_0) depends on the temperature, and the Arrhenius relation is applied to model the dependency:

$$R_0(T) = R_0|T_{amb} + exp\left(\alpha\left(\frac{1}{T_{cell}} - \frac{1}{T_{amb}}\right)\right), \quad \propto= \frac{E}{RT} \tag{6}$$

where α is the Arrhenius rate constant for the polarization resistance.

The main parameters of the implemented battery model are reported in Table 1, as the equivalent electrical circuit including thermal modelling is represented in Figure 2.

Table 1. Main parameters of the retained battery model.

Parameter	Symbol	Value	Unit
Nominal voltage	V_N	51.2	V
Nominal capacity	C_N	25	Ah
Ambient temperature	T_{amb}	298	K
Cell battery mass	m	0.05	kg
Specific heat capacity	c_p	925	J/kgK
Surface area	A	15.3×10^{-3}	m^2
Thermal time constant	τ_{th}	2000	s
Thermal resistance	R_{th}	279	K/W
Horizontal heat transfer coefficient	h	5	$\frac{W}{m^2} \cdot K$

(a)

(b)

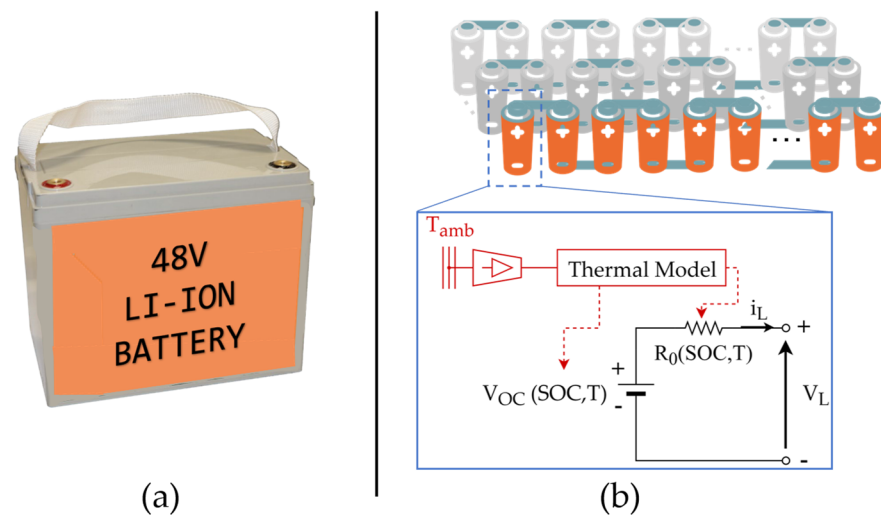**Figure 2.** (**a**) 48 V Battery for the considered HEV; (**b**) equivalent electrical circuit including thermal modelling.

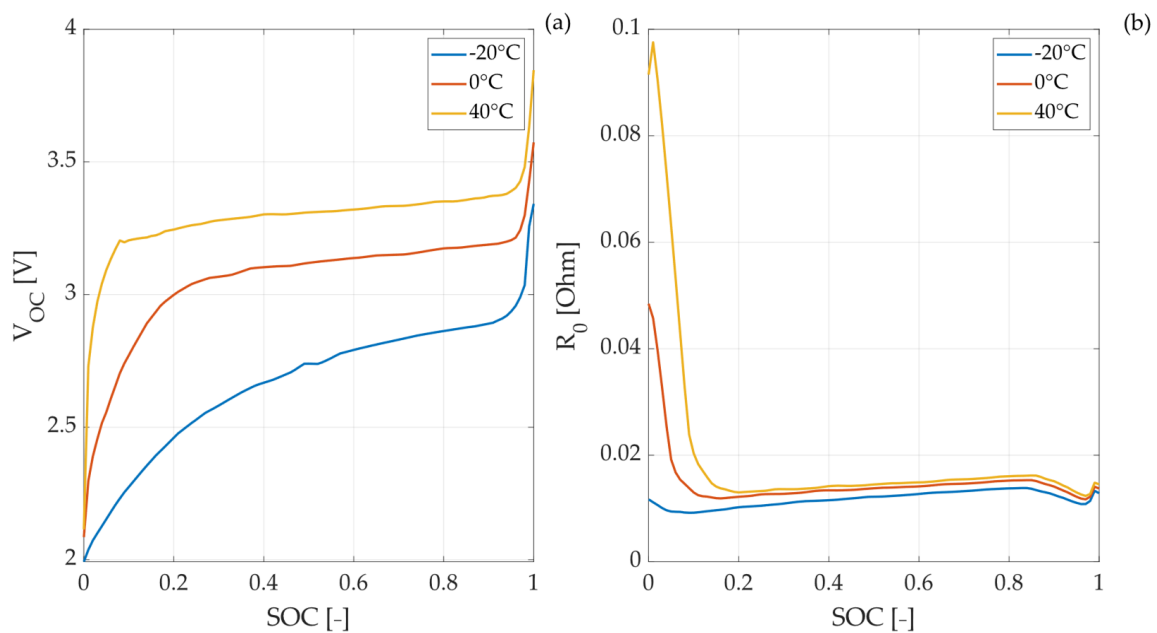The V_{OC} and R_0 characteristics for the considered battery cell are reported in Figure 3.

Figure 3. Battery cell characteristics: (**a**) cell open-circuit voltage V_{OC} vs. *SOC*; (**b**) internal resistance R_0 vs. *SOC*.

2.2. Hardware Setup

Typically, some critical issues arise during the design and real-time implementation of stable, accurate, and robust *SOC* estimation algorithms, such as hysteresis and the flat aspect of the open-circuit controlled voltage $V_{OC} = V_{OC}(SOC, T)$ characteristic curve, lithium-ion battery model, ageing, estimation algorithm selection, and imbalance of the cells. As a result, a HIL validation stage enhances overall software quality and reliability, increases development efficiency, and minimizes systematic software issues.

In this work, HIL is assessed using two different platforms to deploy the battery model and *SOC* estimation method. Specifically, the battery model is deployed on the considered real-time target machine, while the *SOC* estimation method is deployed on the retained evaluation board. The current and voltage signals are sent via UDP protocol between the two platforms. In detail, UDP is a packet-based protocol that uses an Ethernet board as a physical layer. This protocol is advantageous for real-time applications because it has a more negligible delay than TCP connections, since it does not retransmit lost packets. The setup of the HIL test, using the Speedgoat real-time target machine and Raspberry Pi 4B, is shown in Figure 4.
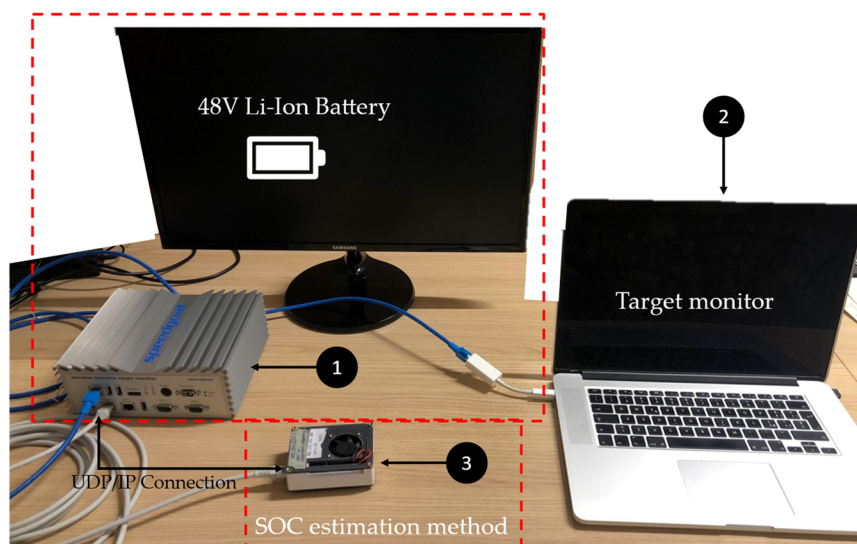

Figure 4. HIL test architecture setup, exploiting UDP/IP connection between host PC and real-time target hardware: (1) Speedgoat baseline real-time target hardware machine; (2) target PC monitor; (3) Raspberry Pi 4B board.

The hardware specifications of the Speedgoat baseline real-time target machine and Raspberry Pi 4B are reported in Table 2.

Table 2. Hardware technical specifications.

	Raspberry Pi 4B	**Speedgoat Baseline**
CPU	Broadcom BCM2711 quad-core Cortex-A72 64-bit SoC @ 1.5 GHz	Intel Celeron 2 GHz 4 cores
Memory	4 GB LPDDR4	4 GB DDR3
Network	Bluetooth 5.0 Gigabit Ethernet	Gigabit Ethernet 2 (Intel I210)
I/O	USB, 40-pin GPIO header	4 × mPCIe
OS	Debian, Raspberry Pi OS	Simulink Real-Time™
Power	5 V DC via USB-C connector	8–36 VDC Input Range

2.3. SOC Estimation Algorithm

In this subsection, the proposed *SOC* estimation algorithm is discussed. Specifically, the training datasets are illustrated, and the ANN architectures are presented and discussed. In particular, two different layouts are analyzed and compared.

The selected ANN architectures are based on a NARX recurrent neural network (RNN) with a feedback connection that encloses several network layers. Because of its simplicity, and the idea that it will operate more accurately in a battery management system, a NARX RNN was selected for this paper. The mathematical model is the following one:

$$y(t) = f\big(y(t-1), y(t-2), \ldots, y(t-n_y), x(t-1), x(t-2), \ldots, x(t-n_x)\big) \qquad (7)$$

where $y(\cdot) \in \mathbb{R}$ is the output, $x(\cdot) \in \mathbb{R}$ are the inputs, and $\big[n_y, n_x\big]$ are the output and inputs buffers, respectively. In the considered model, the next value of the dependent output signal $y(t)$ is regressed on previous values of the output signal and prior values of an independent input signal.

Both the NARX RNN layouts are trained considering a fixed number of hidden layers equal to $L_H = 1$, and the hidden activation function (HAF) is a hyperbolic tangent sigmoid. Moreover, a unique output layer, $L_O = 1$, is also considered, and the corresponding output activation function (OAF) is a linear function.

The training procedure is based on the static Levenberg–Marquardt (LM) backpropagation algorithm for RNN architectures, which is widely used in literature for curve fitting problems, by means of the nonlinear least squares formulation [38–40]. The parameters used in all the training processes are discussed in the following sections.

2.3.1. NARX RNN—Layout 1

The first ANN layout takes, as input, only the current and voltage signals sampled at 10 Hz and returns, at each sample time, the estimated *SOC* value. The detailed NARX RNN structure is reported in Figure 5, while the parameters used during the training process and chosen for the deployment are presented in Table 3. Specifically, the parameters used in the deployment phase are selected during the training phase, after a necessary trial and error heuristic procedure for the accurate minimization of the estimation error.
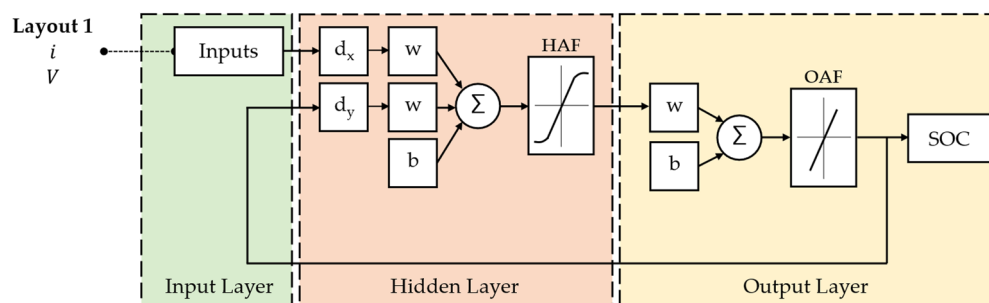

Figure 5. Considered NARX RNN architecture with two inputs.

Table 3. NARX RNN—layout 1: parameters used for training and deployment.

Parameter	Value	
	Training Phase	Deployment Phase
Number of hidden layers	1 to 5	1
Number of neurons/hidden layer	1 to 20	11
Number of epochs	3000	3000
Mean squared error training goal	9×10^{-15}	9×10^{-15}
Min. cost function gradient	9×10^{-12}	9×10^{-12}
Input buffers	0 to 10	0
Output buffers	0 to 10	1

2.3.2. NARX RNN—Layout 2

The chosen structure for the second layout is a NARX RNN with four inputs: voltage, current, averaged terminal voltage, and averaged current at each sample time. The averaged values were computed based on the 500 previous one-second time steps. The use of voltage and current averaged values on a moving window is crucial for two main reasons. Firstly, it reduces the effect of possible estimation error in the output that propagates to the input layer, due to the feedback connection, and it also reduces the *SOC* estimation error, when compared to using only the current and voltage at each time step.

As for layout 1, the detailed NARX RNN structure is reported in Figure 6. The parameters used in all the training and the parameters chosen for the deployment are presented in Table 4. In detail, the parameters used in the deployment phase are selected during the training phase after a necessary trial and error heuristic procedure for accurate minimization of the estimation error.
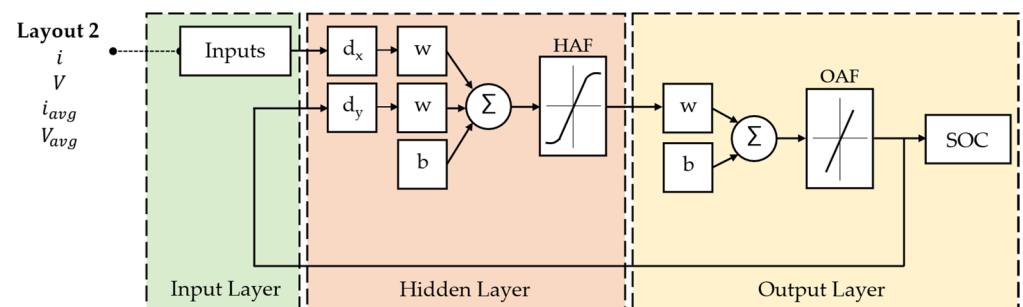

Figure 6. Considered recurrent ANN architecture with four inputs.

Table 4. RNN—Layout 2: parameter values for training and final deployment.

Parameter	Value	
	Training Phase	**Deployment Phase**
Number of hidden layers	1 to 5	1
Number of neurons/hidden layer	1 to 20	6
Number of epochs	3000	3000
Mean squared error training goal	9×10^{-15}	9×10^{-15}
Min. cost function gradient	9×10^{-12}	9×10^{-12}
Input buffers	0 to 10	0:1
Output buffers	0 to 10	1:2

2.4. Training Dataset

When data-driven approaches are considered, the quality of the data used for the training process is strictly linked to the goodness of the resulting RNN. It is straightforward that the training dataset should be, as much as possible, complete and close to the real use-cases.

In this work, the current (subfigure a), voltage (subfigure b), and *SOC* (subfigure c) profiles of the training dataset are displayed in Figure 7 for the first RNN layout, while Figure 8 illustrate the current and averaged current (subfigure a), voltage and averaged voltage (subfigure b), and *SOC* (subfigure c) used for the second RNN layout.
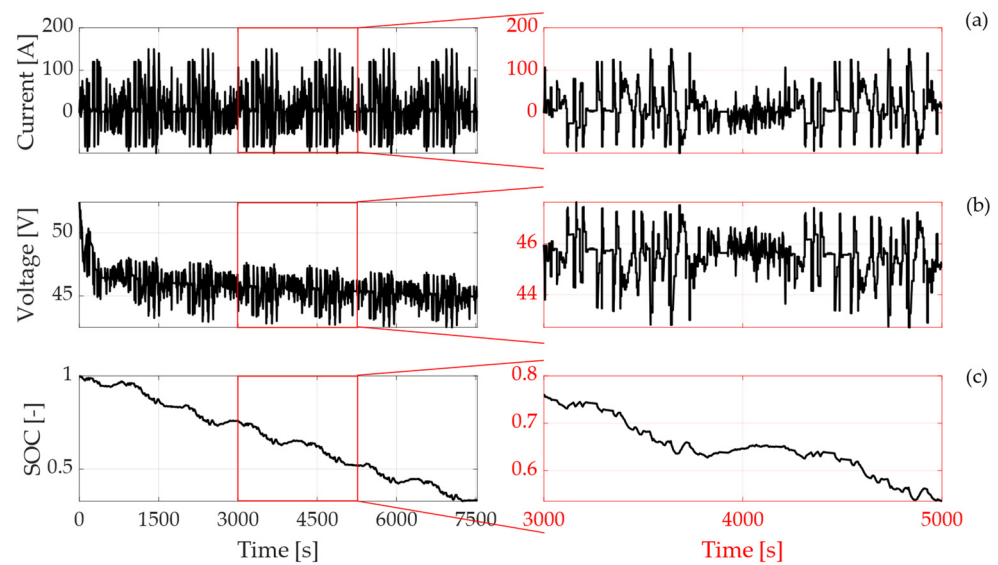
Figure 7. Training dataset for NARX RNN—layout 1: (**a**) current, (**b**) voltage, (**c**) *SOC*.
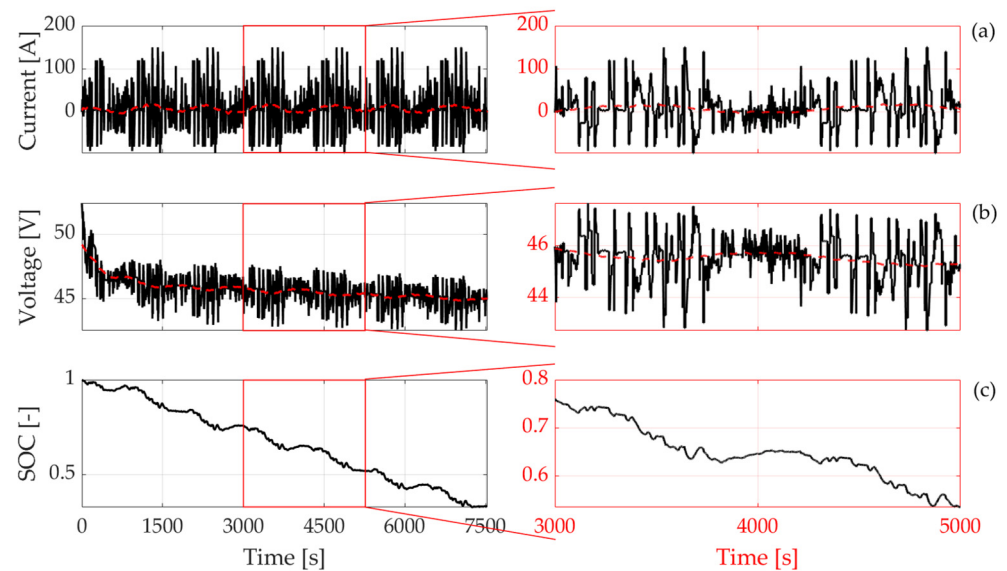

Figure 8. Training dataset for NARX RNN—layout 2: (**a**) current (solid black) and averaged current (dashed red), (**b**) voltage (solid black) and averaged voltage (dashed red), (**c**) *SOC*.

The retained datasets are shown for an amount of time equal to 7532 *s*. Sampling rates of 10 (Hz) are used to sample the modeled data. In this study, each dataset is recorded at a constant temperature of 25 °C, including the datasets under consideration. It is common to divide a training dataset into three parts during the learning phase, in order to assess training performance and avoid overfitting issues [35]. This is done by splitting the training dataset into three parts: training (70% of the full dataset), test (15%), and validation (15%).

Then, the robustness of the actual datasets used for training the retained NARX RNNs is enhanced, including possible errors in signal measurements and, thus, including disturbances in the modeled training data. Specifically, a varying positive/negative additive error is applied to the current signal used in the training dataset, in the range required by the standards for the current probes used in the automotive sector.

3. Results and Discussion

This section presents the results to evaluate the performance of the obtained RNN layouts. The proposed method is tested on charging/discharging profiles aiming to replicate

the daily usage of a 48 V lithium-ion battery for HEVs. The testing datasets, namely A and B, include the measurements of current and voltage, recorded at a constant temperature of 25 °C. Specifically, dataset A refers to a charge-depleting application, while dataset B replicates a charge-sustaining mode in HEVs. The current, averaged current (subfigure a), voltage, and averaged voltage (subfigure b) trends for datasets A and B are shown in Figures 9 and 10, respectively. As for the training dataset, the averaged values are computed based on the 500 previous time steps. In detail, a positive current represents the discharging condition that is usual during driving time, while a negative current considers a charging condition during regenerative braking. Specifically, the current values range from −100 A to 100 A, while the voltage is always in between 43 V and 52 V, which is representative of a fully charge/discharge cycle in the retained application.
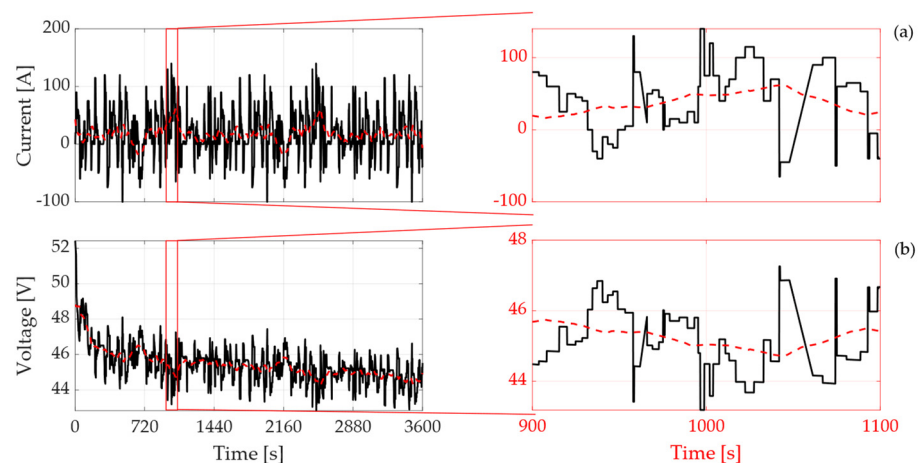

Figure 9. Testing dataset A: (**a**) current (solid black) and averaged current (dashed red), (**b**) voltage (solid black) and averaged voltage (dashed red).
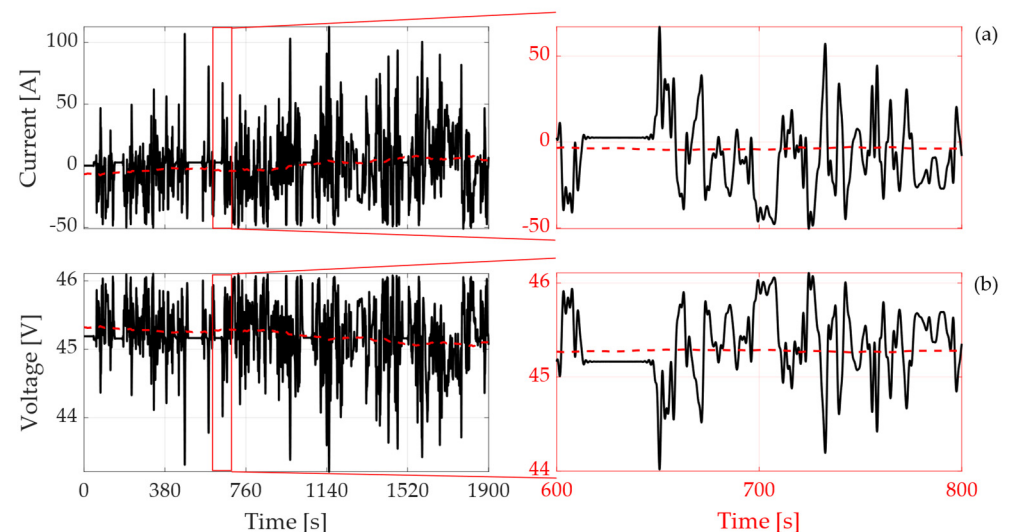

Figure 10. Testing dataset B: (**a**) current (solid black) and averaged current (dashed red), (**b**) voltage (solid black) and averaged voltage (dashed red).

The following subsections discuss the estimation results, when the two different RNN layouts are applied.

3.1. SOC Estimation Results

Figures 11–14 represent the estimation results for the testing datasets A and B, when NARX RNN layouts 1 and 2 were used for the *SOC* estimation, respectively.
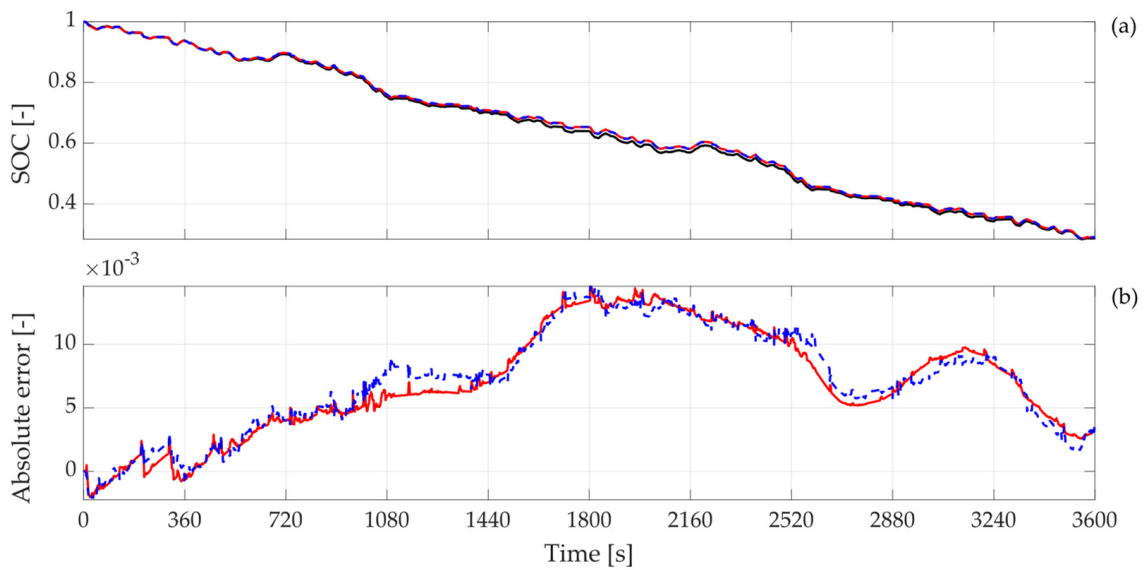
Figure 11. Results on testing dataset A—NARX RNN layout 1: (**a**) reference *SOC* (solid black line) vs. simulation estimated *SOC* (solid red line), HIL estimated *SOC* (blue dashed line) (**b**) simulation absolute error (red solid line), HIL absolute error (blue dashed line).

Figure 12. Results on testing dataset B—NARX RNN layout 1: (**a**) reference *SOC* (solid black line) vs. simulation estimated *SOC* (solid red line), HIL estimated *SOC* (blue dashed line) (**b**) simulation absolute error (red solid line), HIL absolute error (magenta dashed line).
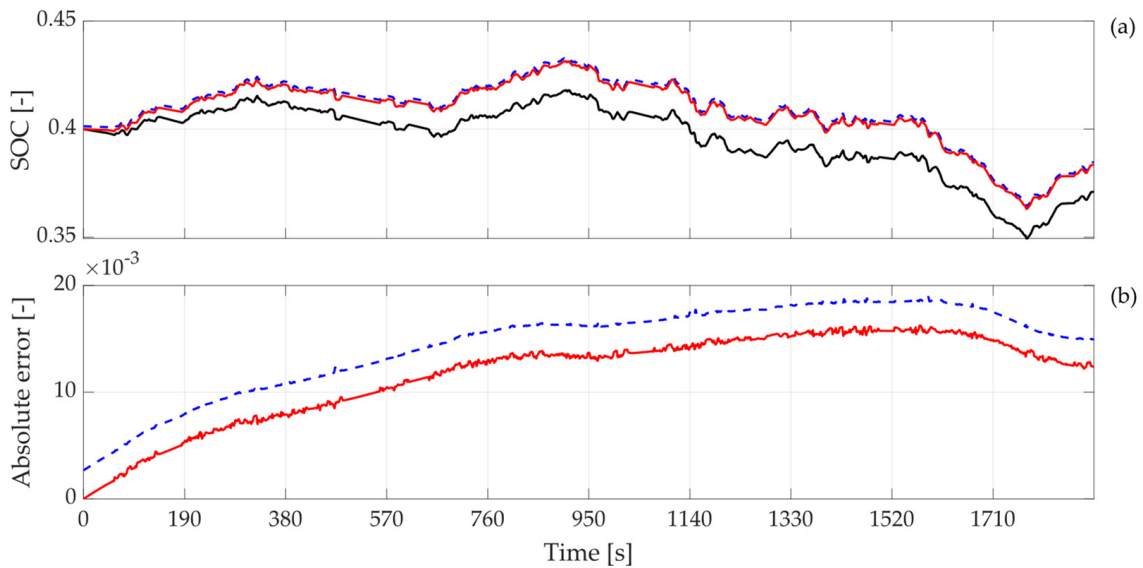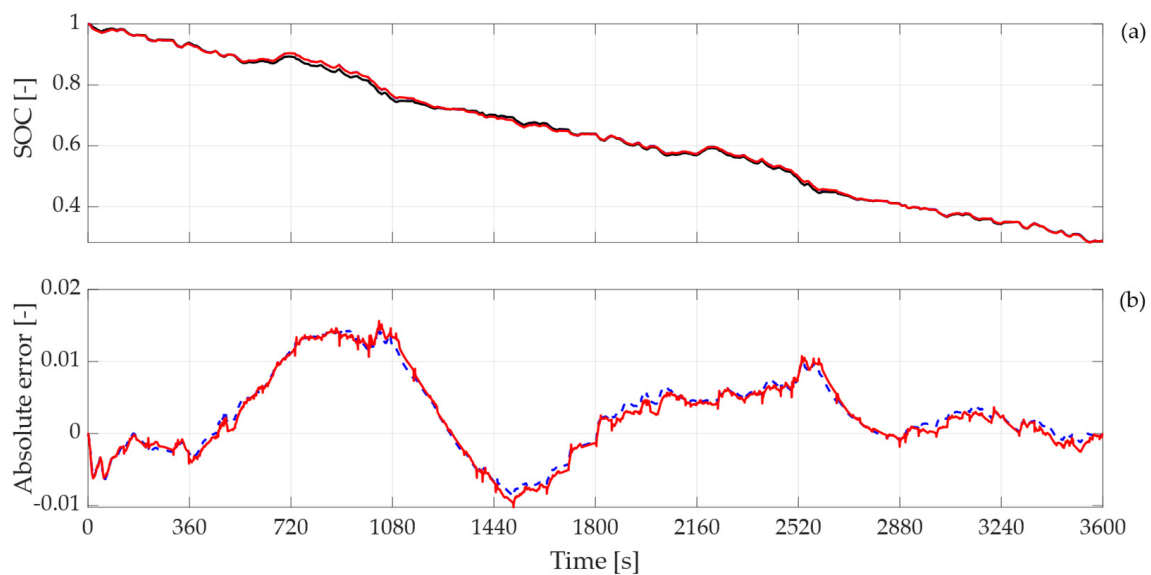
Figure 13. Results on testing dataset A—NARX RNN layout 2: (**a**) reference *SOC* (solid black line) vs. simulation estimated *SOC* (solid red line), HIL estimated *SOC* (blue dashed line) (**b**) absolute simulation error (solid red line), HIL absolute error (blue dashed line).

Figure 14. Results on testing dataset B—NARX RNN layout 2: (**a**) reference *SOC* (solid black line) vs. simulation estimated *SOC* (solid red line), HIL estimated *SOC* (blue dashed line) (**b**) absolute simulation error (solid red line), HIL absolute error (blue dashed line).
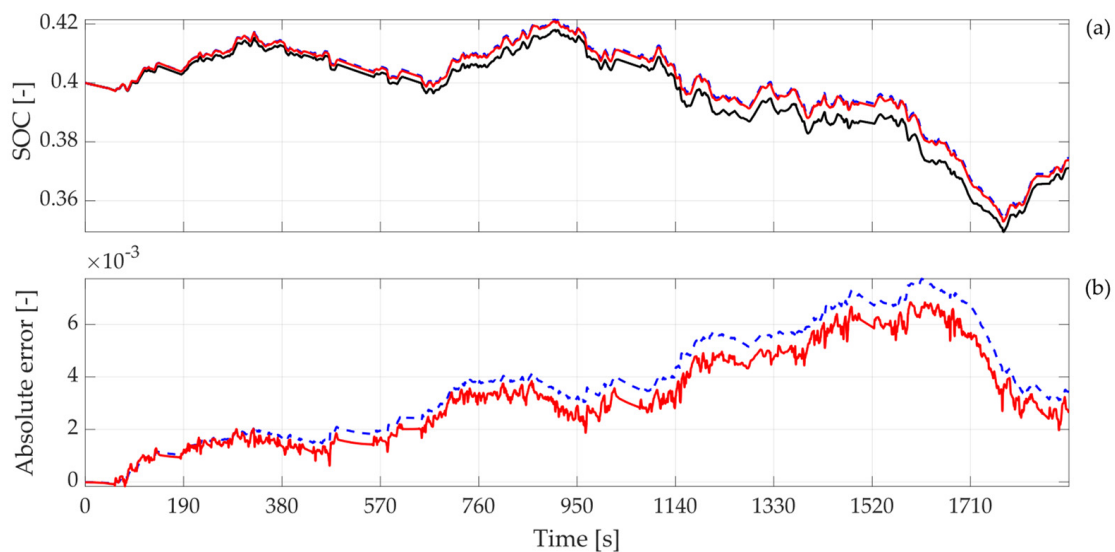
In each figure, subfigures (a) show the reference *SOC* (solid black line) from the numerical battery model, with respect to the *SOC*, estimated both by the ANN-based algorithm in a proper MATLAB/Simulink simulation environment (solid red line) and retained HIL configuration (dashed blue line), respectively.

The *SOC* values range from 1 to 0, where 1 means the battery is totally charged, and 0 indicates the battery is empty. Subfigures (b) show the absolute errors between the reference *SOC* and the estimated *SOC*, in both the simulation environment and the HIL configuration.

Figures 11 and 12 refer to the NARX RNN layout 1; thus, the averaged values of current and voltage have not been taken into account. As shown in the figures, the *SOC* estimation is more accurate when dataset A is considered. Indeed, testing dataset A simulates a use-case similar to the one reported in the training dataset. However, even if

the estimation error is bigger for testing dataset B, the estimation errors are generally quite low and always below 2%.

Figures 13 and 14 refer to NARX RNN layout 2, in which the averaged values of current and voltage are two additional inputs for the algorithm. The averaged values are computed over a sliding window of 500 time steps, as performed in the training phase. In contrast to layout 1, the *SOC* estimation is more accurate, while considering the testing of dataset B. Nevertheless, the estimation errors are generally lower, with respect to the ones recorded for layout 1, as they are always below 1.5%.

3.2. Performance Analysis

The obtained results are evaluated, in terms of mean square prediction error (MSPE) and maximum absolute prediction error (MAPE), which are defined in the following equations, respectively:

$$MSPE = 1/N \sum_{i=1}^{N} (y_i - \bar{y}_i)^2 \tag{8}$$

$$MAPE = max(y - \bar{y}) \tag{9}$$

where N is the number of samples, $\bar{y}$ the reference output, and y the estimated value. The outcomes of the performed estimation accuracy analysis are reported in Table 5.

Table 5. Estimation accuracy analysis, in terms of MSPE and MAPE.

Layout		Error	Dataset A	Dataset B
Layout 1	Simulation	MSPE	6.51×10^{-5}	1.54×10^{-4}
		MAPE	1.46×10^{-2}	1.64×10^{-2}
	HIL	MSPE	6.74×10^{-5}	1.99×10^{-4}
		MAPE	1.48×10^{-2}	1.81×10^{-2}
Layout 2	Simulation	MSPE	3.74×10^{-5}	1.33×10^{-5}
		MAPE	1.42×10^{-2}	0.68×10^{-2}
	HIL	MSPE	3.83×10^{-5}	1.81×10^{-5}
		MAPE	1.46×10^{-2}	0.77×10^{-2}

In detail, the analysis is performed for both the considered ANN layouts, and it is conducted both for the simulation environment and for the HIL validation. The results highlight that layout 2 is accurate in estimating the *SOC* in testing datasets A and B. Moreover, focusing on layout 1, which means that the averaged values of the current and voltage are not considered, the estimation accuracy is higher in dataset A, with respect to dataset B. This is because the training dataset is even more similar to the testing dataset A. Therefore, the layout 1 is less responsive to the different dynamics in dataset B, even though the MAPE values are always below 2% in the simulation environment and HIL validation and the MSPE values are quite low, in between 10^{-5} and 10^{-4}. Furthermore, layout 2, which also considers the current and voltage average values, shows better performance in MAPE and MSPE for both the testing datasets. The MAPE values are significantly low and, especially in dataset B, they are less than 1%, both in simulation and HIL testing configurations. The computed MSPE values are fairly negligible, as they are between 10^{-6} and 10^{-5}.

4. Conclusions

This paper presents the design and HIL assessment of a data-driven method for *SOC* estimation in lithium-ion batteries. The study was specifically conducted to evaluate the feasibility of the investigated algorithm in an industrial-grade framework, using state-of-the-art, real-time hardware, such as Raspberry Pi 4B and Speedgoat baseline, which have been connected via UDP protocol.

Specifically, the novel contribution of this work is the experimental validation of the proposed estimation method in a HIL configuration. The investigated method is specifically

aimed at mild HEVs, and various real-world driving cycles, related to this application, were used to test the retained algorithms.

A lithium-ion battery that is used in real HEVs has been modeled, via an equivalent RC model, considering thermal influence to generate both training and validation datasets. Indeed, the retained ANNs have been trained and tested with driving cycles obtained from HEVs applications, during charge-sustaining and -depleting cycles. In detail, two alternative estimation architectures have been designed and compared during the validation procedure, in terms of estimation performance. Both are based on the NARX model that is implemented via ANNs. In terms of mean percentage error, the resulting estimation algorithm can estimate the battery *SOC* in real-time with 2% accuracy.

The proposed HIL architecture demonstrated that the estimation algorithm can provide relevant results within the investigated experimental framework, ensuring that the proposed data-driven algorithm, based on NARX ANNs, can be rapidly deployed, tested, and validated on state-of-the-art hardware platforms. This approach could ease the implementation on actual automotive ECUs used in the automotive industry. A further extensive experimental validation phase is needed before generalization of the approach to any automotive ECU, provided that a wide experimental campaign is conducted.

References

1. Ehsani, M.; Singh, K.V.; Bansal, H.O.; Mehrjardi, R.T. *State of the Art and Trends in Electric and Hybrid Electric Vehicles*; IEEE: Piscataway, NJ, USA, 2021; Volume 109, pp. 967–984.
2. Bishop, J.; Martin, N.P.; Boies, A.M. Cost-effectiveness of alternative powertrains for reduced energy use and CO_2 emissions in passenger vehicles. *Appl. Energy* **2014**, *124*, 44–61. [CrossRef]
3. Anderman, M. *Status and Trends in the HEV/PHEC/EV Battery Industry*; Rocky Mountain Institute: Snowmass, CO, USA, 2008.
4. Chen, X.; Shen, W.; Vo, T.T.; Cao, Z.; Kapor, A. An Overview of Lithiumion Batteries for Electric Vehicles. In Proceedings of the IEEE IPEC Conference on Power and Energy, Ho Chi Minh City, Vietnam, 12–14 December 2012.
5. Van Mierlo, J.; Berecibar, M.; El Baghdadi, M.; De Cauwer, C.; Messagie, M.; Coosemans, T.; Jacobs, V.; Hegazy, O. Beyond the State of the Art of Electric Vehicles: A Fact-Based Paper of the Current and Prospective Electric Vehicle Technologies. *World Electr. Veh. J.* **2021**, *12*, 20. [CrossRef]
6. Bonfitto, A.; Ezemobi, E.; Amati, N.; Feraco, S.; Tonoli, A.; Hegde, S. State of Health Estimation of Lithium Batteries for Automotive Applications with Artificial Neural Networks. In Proceedings of the 2019 AEIT International Conference of Electrical and Electronic Technologies for Automotive (AEIT AUTOMOTIVE), Turin, Italy, 2–4 July 2019; pp. 1–5.
7. Cardoso, D.S.; Fael, P.O.; Espírito-Santo, A. A review of micro and mild hybrid systems. *Energy Rep.* **2019**, *6*, 385–390. [CrossRef]
8. Lo, E.W. Review on the configurations of hybrid electric vehicles. In Proceedings of the 2009 3rd International Conference on Power Electronics Systems and Applications (PESA), Hong Kong, 20–22 May 2009; pp. 1–4.
9. Sabri, M.M.; Danapalasingam, K.; Rahmat, M. A review on hybrid electric vehicles architecture and energy management strategies. *Renew. Sustain. Energy Rev.* **2016**, *53*, 1433–1442. [CrossRef]
10. Jayakumar, A.; Chalmers, A.; Lie, T.T. Review of prospects for adoption of fuel cell electric vehicles in New Zealand. *IET Electr. Syst. Transp.* **2017**, *7*, 259–266. [CrossRef]
11. Lee, S.R.; Choi, B.Y.; Lee, J.Y.; Won, C.Y. 48 V to 12 V soft-switching interleaved buck and boost converter for mild-hybrid vehicle application. In Proceedings of the 2016 19th International Conference on Electrical Machines and Systems (ICEMS), Chiba, Japan, 13–16 November 2016; pp. 1–6.
12. Leksono, E.; Haq, I.N.; Iqbal, M.; Soelami, F.N.; Merthayasa, I. State of Charge (SoC) Estimation on LiFePO4 Battery Module Using Coulomb Counting Methods with Modified Peukert. In Proceedings of the IEEE 2013 Joint International Conference on Rural Information & Communication Technology and Electric-Vehicle Technology, Bandung, Indonesia, 26–28 November 2013.

13. Chang, W.-Y. The State of Charge Estimating Methods for Battery: A Review. *ISRN Appl. Math.* **2013**, *2013*, 1–7. [CrossRef]
14. Rivera-Barrera, J.P.; Muñoz-Galeano, N.; Sarmiento-Maldonado, H.O. SoC Estimation for Lithium-ion Batteries: Review and Future Challenges. *Electronics* **2017**, *6*, 102. [CrossRef]
15. Wei, Z.; Zhao, J.; Ji, D.; Tseng, K.J. A multi-timescale estimator for battery state of charge and capacity dual estimation based on an online identified model. *Appl. Energy* **2017**, *204*, 1264–1274. [CrossRef]
16. Charkhgard, M.; Farrokhi, M. State-of-Charge Estimation for Lithium-Ion Batteries Using Neural Networks and EKF. *IEEE Trans. Ind. Electron.* **2010**, *57*, 4178–4187. [CrossRef]
17. Jiang, C.; Taylor, A.; Duan, C.; Bai, K. Extended Kalman Filter based battery state of charge (SOC) estimation for electric vehicles. In Proceedings of the IEEE Transportation Electrification Conference and EXPO (ITEC), Detroit, MI, USA, 16–19 June 2013.
18. Pérez, G.; Garmendia, M.; Reynaud, J.F.; Crego, J.; Viscarret, U. Enhanced closed loop State of Charge estimator for lithium-ion batteries based on Extended Kalman Filter. *Appl. Energy* **2015**, *155*, 834–845. [CrossRef]
19. Wang, S.; Fernandez, C.; Shang, L.; Li, Z.; Li, J. Online state of charge estimation for the aerial lithium-ion battery packs based on the improved extended Kalman filter method. *J. Energy Storage* **2017**, *9*, 69–83. [CrossRef]
20. He, Z.; Chen, D.; Pan, C.; Chen, L.; Wang, S. State of charge estimation of power Li-ion batteries using a hybrid estimation algo-rithm based on UKF. *Electrochim. Acta* **2016**, *211*, 101–109.
21. Yu, Q.; Xiong, R.; Lin, C. Online Estimation of State-of-charge Based on the H infinity and Unscented Kalman Filters for Lithium-Ion Batteries. *Energy Procedia* **2017**, *105*, 2791–2796. [CrossRef]
22. Ye, M.; Guo, H.; Xiong, R.; Yang, R. Model-based state-of-charge estimation approach of the Lithium-ion battery using an im-proved adaptive particle filter. *Energy Procedia* **2016**, *103*, 394–399. [CrossRef]
23. Kim, T.; Wang, Y.; Sahinoglu, Z.; Wada, T.; Hara, S.; Qiao, W. State of Charge Estimation Based on a Realtime Battery Model and Iterative Smooth Variable Structure Filter. In Proceedings of the IEEE Innovative Smart Grid Technologies—Asia, Kuala Lumpur, Malaysia, 20–23 May 2014.
24. Zou, Z.; Xu, J.; Mi, C.; Cao, B.; Chen, Z. Evaluation of Model Based State of Charge Estimation Methods for Lithium-Ion Batteries. *Energies* **2014**, *7*, 5065–5082. [CrossRef]
25. Du, J.; Liu, Z.; Wang, Y.; Wen, C. A Fuzzy Logic-based Model for Li-ion Battery with SOC and Temperature Effect. In Proceedings of the 11th IEEE Conference on Control & Automation (ICCA), Taichung, Taiwan, 18–20 June 2014.
26. Li, I.-H.; Wang, W.-Y.; Su, S.-F.; Lee, Y.-S. A Merged Fuzzy Neural Network and Its Applications in Battery State-of-Charge Estimation. *IEEE Trans. Energy Convers.* **2007**, *22*, 697–708. [CrossRef]
27. Lin, F.-J.; Huang, M.-S.; Yeh, P.-Y.; Tsai, H.-C.; Kuan, C.-H. DSP-Based Probabilistic Fuzzy Neural Network Control for Li-Ion Battery Charger. *IEEE Trans. Power Electron.* **2012**, *27*, 3782–3794. [CrossRef]
28. Bonfitto, A.; Feraco, S.; Tonoli, A.; Amati, N.; Monti, F. Estimation Accuracy and Computational Cost Analysis of Arti-ficial Neural Networks for State of Charge Estimation in Lithium Batteries. *Batteries* **2019**, *5*, 47. [CrossRef]
29. Vidal, C.; Malysz, P.; Kollmeyer, P.; Emadi, A. Machine Learning Applied to Electrified Vehicle Battery State of Charge and State of Health Estimation: State-of-the-Art. *IEEE Access* **2020**, *8*, 52796–52814. [CrossRef]
30. Zhang, W.; Li, X.; Ma, H.; Luo, Z.; Li, X. Transfer learning using deep representation regularization in remaining useful life prediction across operating conditions. *Reliab. Eng. Syst. Safety* **2021**, *211*, 107556. [CrossRef]
31. Zhang, W.; Li, X.; Li, X. Deep learning-based prognostic approach for lithium-ion batteries with adaptive time-series prediction and on-line validation. *Measurement* **2020**, *164*, 108052. [CrossRef]
32. Vidal, C.; Kollmeyer, P.; Naguib, M.; Malysz, P.; Gross, O.; Emadi, A. Robust xev battery state-of-charge estimator design using a feedforward deep neural network. *SAE Int. J. Adv. Curr. Pract. Mobil.* **2020**, *2*, 2872–2880.
33. He, W.; Williard, N.; Chen, C.; Pecht, M. State of charge estimation for Li-ion batteries using neural network modeling and unscented Kalman filter-based error cancellation. *Int. J. Electr. Power Energy Syst.* **2014**, *62*, 783–791. [CrossRef]
34. Venugopal, P. State-of-Health estimation of li-ion batteries in electric vehicle using IndRNN under variable load condition. *Energies* **2019**, *12*, 4338. [CrossRef]
35. Ceven, S.; Bayir, R. Implementation of Hardware-in-the-Loop Based Platform for Real-time Battery State of Charge Estimation on Li-Ion Batteries of Electric Vehicles using Multilayer Perceptron. *Int. J. Intell. Syst. Appl. Eng.* **2020**, *8*, 195–205. [CrossRef]
36. Tudoroiu, R.E.; Zaheeruddin, M.; Tudoroiu, N.; Radu, S.M. SOC Estimation of a Rechargeable Li-Ion Battery Used in Fuel-Cell Hybrid Electric Vehicles—Comparative Study of Accuracy and Robustness Performance Based on Statistical Criteria. Part I: Equivalent Models. *Batteries* **2020**, *6*, 42. [CrossRef]
37. Huria, T.; Ceraolo, M.; Gazzarri, J.; Jackey, R. High fidelity electrical model with thermal dependence for char-acterization and simulation of high power lithium battery cells. In Proceedings of the 2012 IEEE International Electric Vehicle Conference, Greenville, SC, USA, 4–8 March 2012; pp. 1–8.
38. Levenberg, K. A method for the solution of certain non-linear problems in least squares. *Q. Appl. Math.* **1944**, *2*, 164–168. [CrossRef]
39. Marquardt, D.W. An Algorithm for Least-Squares Estimation of Nonlinear Parameters. *J. Soc. Ind. Appl. Math.* **1963**, *11*, 431–441. [CrossRef]
40. Tetko, I.V.; Livingstone, D.J.; Luik, A.I. Neural network studies. 1. Comparison of overfitting and overtraining. *J. Chem. Inform. Comput. Sci.* **1995**, *35*, 826–833. [CrossRef]